

Unit Cell Structure of Crystal Polytypes in InAs and InSb Nanowires

Dominik Kriegner,^{*,†} Christian Panse,^{*,‡} Bernhard Mandl,^{†,§} Kimberly A. Dick,^{§,||} Mario Keplinger,[†] Johan M. Persson,[⊥] Philippe Caroff,^{‡,§} Daniele Ercolani,^{||} Lucia Sorba,^{||} Friedhelm Bechstedt,[‡] Julian Stangl,[†] and Günther Bauer[†]

[†]Institute of Semiconductor and Solid State Physics, Johannes Kepler University Linz, Altenbergerstrasse 69 A-4040 Linz, Austria

[‡]Institut für Festkörpertheorie und -optik, Friedrich-Schiller-Universität Jena, Max-Wien-Platz 1, D-07743 Jena, Germany

[§]Solid State Physics, Lund University, Box 118, S-22100 Lund, Sweden

^{||}Polymer & Materials Chemistry, Lund University, Box 124, S-22100 Lund, Sweden

[⊥]Center for Electron Nanoscopy, Technical University of Denmark, Fysikvej, building 307, DK-2800 Kgs Lyngby, Denmark

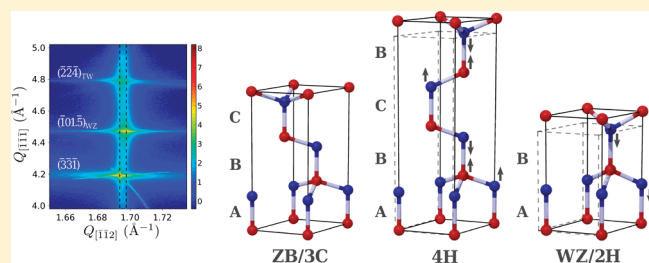
^{*}IEMN, UMR CNRS 8520, BP 60069, Avenue Poincaré, 59652 Villeneuve d'Ascq, France

^{||}NEST, Istituto Nanoscienze-CNR and Scuola Normale Superiore, Piazza S. Silvestro 12, I-56127 Pisa, Italy

S Supporting Information

ABSTRACT: The atomic distances in hexagonal polytypes of III–V compound semiconductors differ from the values expected from simply a change of the stacking sequence of (111) lattice planes. While these changes were difficult to quantify so far, we accurately determine the lattice parameters of zinc blende, wurtzite, and 4H polytypes for InAs and InSb nanowires, using X-ray diffraction and transmission electron microscopy. The results are compared to density functional theory calculations. Experiment and theory show that the occurrence of hexagonal bilayers tends to stretch the distances of atomic layers parallel to the c axis and to reduce the in-plane distances compared to those in zinc blende. The change of the lattice parameters scales linearly with the hexagonality of the polytype, defined as the fraction of bilayers with hexagonal character within one unit cell.

KEYWORDS: Nanowires, polytypes, crystal structure, X-ray diffraction, density functional theory



Nanowires (NWs) are promising candidates for future electronic and optoelectronic devices.^{1,2} In NWs, the formation of different crystal structure polytypes is a common phenomenon.^{3–10} One reason for the presence of different polytypes in NWs is that the atomic layers have the same in-plane structure with respect to the most common $\langle 111 \rangle$ B growth directions. Only the stacking sequence along the growth direction differs, and it often changes during growth along the $[\bar{1}\bar{1}\bar{1}]$ direction. The stacking is ABCABC... for the zinc blende (ZB) structure and ABAB... for the most common hexagonal polytype, the wurtzite (WZ) structure, and ABCBACB... for the 4H structure. Each of the letters A, B, and C corresponds to a bilayer of atoms, consisting of one layer with group III and one with group V atoms. So far, most nanowire growth schemes produced a rather random sequence of polytypes, with a high density of various stacking defects. Only recently several groups have demonstrated controlled growth of nanowires with specific lattice structure.^{3,6,7,11–14} Since the electronic band structure is linked to the lattice structure, this enables the fabrication of polytypic heterostructures within the *same material*, like polytypic superlattices.^{15,16} Consequently, a thorough investigation of the crystal structure is timely, to enable corresponding studies on the band structure and band alignment. Up to now only few groups have considered this,

often in a semiquantitative way due to lack of precise structural data.^{4,17–20} For a complete understanding, also the influence of strains emerging due to the stacking of different crystal polytypes needs to be taken into account.

It is often assumed that the lattice constants of the hexagonal polytypes can be derived from geometric conversion of the cubic bulk lattice constant, e.g., by shifting layers from the cubic to the hexagonal close-packed arrangement. For an ideal WZ lattice this means that the lattice constants $c_{\text{geom,WZ}}$ and $a_{\text{geom,WZ}}$ along the cubic $[111]$ direction and within the plane spanned by $[\bar{1}\bar{1}0]$ and $[\bar{1}1\bar{2}]$ are related to the cubic lattice constant a_c via $c_{\text{geom,WZ}} = a_c(4/3)^{1/2}$ and $a_{\text{geom,WZ}} = a_c/2^{1/2}$. The conversion neglects that distortions of the bonding tetrahedra are common in hexagonal polytypes,²¹ and indeed, many research groups have found deviations from this assumption of ideal bonding tetrahedra, finding slightly different lattice parameters both in growth direction and in the growth plane. This means that the ideal relation $c_{\text{WZ}}/a_{\text{WZ}} = (8/3)^{1/2}$ is not anymore fulfilled. The particular values for the

Received: November 29, 2010

Revised: February 10, 2011

Published: March 24, 2011

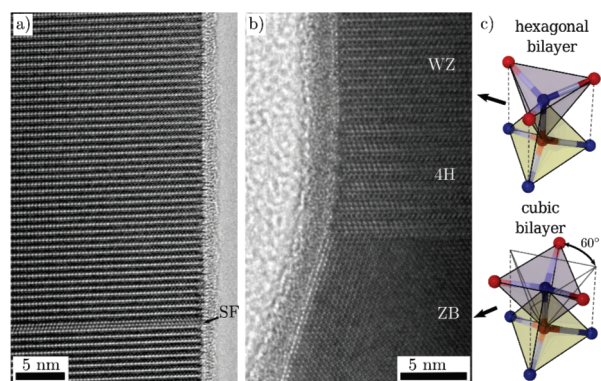


Figure 1. Transmission electron micrograph of an InAs wire (a) and an InSb wire (b) and a sketch of hexagonal and cubic stacked layers (c). In (a) a part of a wire from sample A1, which consists mainly of the WZ structure with some stacking faults (SF), is shown. In (b) from bottom to top the ZB, 4H, and WZ phase in a wire from sample E2 is shown. Both images were recorded in $[1\bar{1}0]$ zone axis. Panel c shows the different stacking/bond configuration of a cubic and a hexagonal bilayer. Whereas the upper group III atoms (red) are located above the group V (blue) atoms in the hexagonal case, they are located at an rotated position in the cubic case.

lattice parameters of WZ InAs^{22–25} differ, however, considerably between the different studies. The reason for these discrepancies is most probably that in most growth schemes of NWs the resulting polytype structure is not well controlled, leading to wires with a more or less random sequence of cubic ZB and hexagonal WZ segments and possibly also with more complex stacking forms, resulting in other polytypes like 4H. In addition, the wires often contain a high density of defects such as stacking faults and twin boundaries. As a result, the individual segments of the wires are often mutually strained, and it is difficult or even impossible to extract the “true bulk” lattice parameters of the individual polytypes from measurements of such samples.

In this work, we present precise systematic studies of the variations of the unit cell parameters of InAs and InSb for ZB, WZ and 4H in NWs. We employ high-resolution X-ray diffraction (XRD) on samples with controlled crystal phase and compare the obtained lattice parameters to results of density functional theory (DFT) calculations. We can show that deviations from the simple geometric conversion formula indeed exist and determine the real lattice constants for hexagonal polytypes of InAs and InSb. To be able to determine the lattice constants a and c for WZ, and other hexagonal polytypes, NWs with low defect density and sufficiently long single phase segments are required. Transmission electron microscopy (TEM) was used to select suitable samples, since the microscopic arrangement of the different crystal phases cannot be obtained from the XRD data directly.

The III–V bilayers in $[000.\bar{1}][111]$ direction²⁶ can have cubic or hexagonal character depending on the stacking A, B, or C of the neighboring layers: In the cubic case, the layers above and below the considered layer are of different type, e.g., a B layer has an A and a C layer as neighbors. In the hexagonal case, the neighboring layers are of the same type, e.g., a B layer has two A layers as neighbors. In the ZB structure, all bilayers therefore have cubic character as shown in Figure 1c. Since the periodicity in $[111]$ direction is reached after three bilayers, this structure is also termed 3C. In the WZ geometry, the periodicity amounts to two bilayers with hexagonal character (Figure 1c), therefore also denoted as 2H. The 4H polytype has a periodicity of four bilayers with mixed character. Polytypes with

even larger unit cells are possible, e.g., 6H with a ABCACBAB-CACB... stacking sequence. The total number of III–V bilayers in the unit cell of an pH/pC polytype is given by p . The ratio of the number of hexagonal stacked bilayers to the total number of bilayers (p) gives the percentage of hexagonality, which is 0% for ZB/3C, 33% for 6H, 50% for 4H, and 100% for WZ/2H. The results will be discussed as a function of the hexagonality. The atomic structure and electronic structure are intimately connected and mutually influence each other.^{15,27,28} This self-consistency leads to the actual atomic positions for a given bilayer stacking and hence III–V polytype and is defined by vanishing Hellmann–Feynman forces,²⁹ the gradients of the total energy in DFT calculations with respect to the atomic positions. As a result, not only the unit cell dimensions a and c of a polytype but also the so-called cell internal parameters can be calculated. They describe deformations of the bonding tetrahedra, leading to slight displacements of the atom positions *within the unit cell*. Since theory reveals the reasons of geometrical variations, a comparison with numerical data contributes to a better understanding of these variations as a function of the bilayer stacking.

For several tetrahedrally coordinated II–VI and III–V compounds, where both ZB and WZ modifications were available, systematic deviations for bulk structures were already found experimentally back in the 1970s.³⁰ For compounds where the cubic phase is the stable one under ambient conditions, the ratio c_{WZ}/a_{WZ} was found to be larger than the ideal $(8/3)^{1/2}$ for the WZ phase,³⁰ in qualitative agreement with our findings below and those reported on polycrystalline bulk GaAs–WZ³¹ as well as theoretical predictions.^{32,33} For bulk GaAs the WZ phase could only be realized by starting from GaAs in its ZB phase and transforming it at high hydrostatic pressures of 24 GPa first into an orthorhombic phase. Subsequent heat treatment and pressure reduction to about 14 GPa resulted in a SC16 phase which transformed after a further heat treatment at ambient conditions completely into the WZ phase.³¹ From high-resolution X-ray diffraction a c_{WZ}/a_{WZ} ratio of about 1.645 was reported by McMahon et al.;³¹ this ratio turned out to be independent of pressure up to 20 GPa.

A precise study of the lattice parameters of the hexagonal polytypes of InAs and InSb became only possible due to availability of those materials in the form of NWs. The growth of NWs with different polytypes further allows for the design of polytypic heterostructures, which are not possible to produce by pressure treatment.

Since the reported deviations between WZ and ZB structure are only in the order of 0.2–0.5% of the lattice parameters, in the present work special care was taken to exclude growth-specific effects, e.g., from dopants, and systematic measurement errors, by investigating selected samples obtained from different growth methods and by comparing the results obtained using different XRD setups. The small absolute deviations of the lattice parameters also represent a challenge for the numerical convergence of the DFT calculations.

We investigated several series of InAs and InSb nanowire samples, grown using metal organic vapor phase epitaxy (MOVPE), and for comparison InAs nanowires grown by chemical beam epitaxy (CBE). We selected samples under the condition that wires are fabricated as pure as possible in terms of the polytypism and that in addition the density of defects (stacking faults, twin planes) is very low. All samples were grown on InAs (111) B substrates. The CBE growth of the InAs wire samples A1 and A2 was performed, using catalyst particles formed by thermally dewetting of a ~ 5 Å thick Au film.³⁴ The CBE growth system employs pressure control in the precursor lines to set the trimethylindium (TMIn) and the tertiarybutylarsine (TBAs) fluxes. TBAs is thermally cracked at 1000 °C in

Table 1. List of Samples Together with Their Characteristics (NW Material and Growth Method)^a

sample name	NW material	growth method	seed method
A1–A2	InAs	CBE	Au film
B1	InAs	CBE	60 nm; $1.0 \mu\text{m}^{-2}$
C1	InAs	MOVPE	45 nm; $0.5 \mu\text{m}^{-2}$
C2	InAs	MOVPE	25 nm; $0.5 \mu\text{m}^{-2}$
C3	InAs	MOVPE	45 nm; $1.0 \mu\text{m}^{-2}$
D1	InAs	MOVPE	45 nm; $0.5 \mu\text{m}^{-2}$
D2	InAs	MOVPE	50 nm; $1.0 \mu\text{m}^{-2}$
D3	InAs	MOVPE	55 nm; $0.5 \mu\text{m}^{-2}$
E1–E2	InSb	MOVPE	self-seeded

^a All samples were grown on InAs (111)B substrates. Au particles with given diameter and area density were used as seed particles except for samples A and E.

the injector. Nanowires were grown at 420 °C with the line pressures set to 0.6, 0.4 and 1.33, 2.66 mbar for TMIn and TBAs, respectively, for samples A1, A2. For sample B1 a substrate decorated by size-controlled gold seed particles³⁵ was used: CBE growth was performed at 419 °C using TMIn and TBAs as group III and V supply at pressures of 0.15 and 1.5 mbar, respectively. TBAs were thermally precracked before introducing into the growth chamber. The MOVPE growth of InAs wires (samples C and D) was performed on substrates decorated with size-controlled gold seed particles in a standard MOVPE reactor (pressure of 100 mbar, total reactor flow 13 L/min). For the wurtzite phase, the growth temperature was set to 410 °C, for the zinc blende phase it was 380 °C, with V/III ratios of 28 and 123, respectively. The TMIn molar fraction was kept constant at 6.9×10^{-6} for both crystal phases, and the arsine supply was adjusted accordingly.^{6,7} InSb wires (samples E) were fabricated using MOVPE on substrates covered with an ultrathin SiO_x layer ($x \approx 1$, ~ 13 Å thick) in a self-seeded vapor liquid solid mechanism.³⁶ The nominal molar fractions used were 5.5×10^{-6} and 4.2×10^{-5} for TMIn and trimethylantimony, respectively. The samples were annealed at 580 °C, and growth was performed at 440 °C and stopped by turning off the indium supply.⁸ In all cases no precursors other than those needed for the III–V compound growth were supplied to ensure the presence of pure InAs and InSb NWs and hence to exclude influences, e.g., from dopants.⁹ Table 1 contains an overview of the samples and lists the different seed methods used for the growth.

The length of WZ, ZB, and 4H segments as well as the defect density was characterized for all samples using TEM. Typical high-resolution images are shown in Figure 1 for InAs (sample A1) and InSb (sample E2) NWs. TEM confirmed the presence of well-separated ZB, 4H, and WZ parts for the InSb samples, whereas two different sets of samples were used to determine WZ (samples A, B, and C) and ZB (samples D) lattice parameters for InAs. While the particular structure of the individual samples differs, the selected samples have in common that they contain extended pure (almost defect-free) WZ and/or ZB segments. While all investigated InSb samples contain 4H segments, the 4H structure has only been observed in sample C1 for InAs. For both, InAs and InSb wires, the 4H segments are rather short and “sandwiched” between ZB and WZ. Neither for InAs nor for InSb wires was a 6H structure observed.

These samples give us the unique possibility to determine the fully relaxed lattice constants of the WZ and ZB phases. To be able to determine the lattice constants a and c for the hexagonal polytypes, X-ray diffraction measurements along the crystal

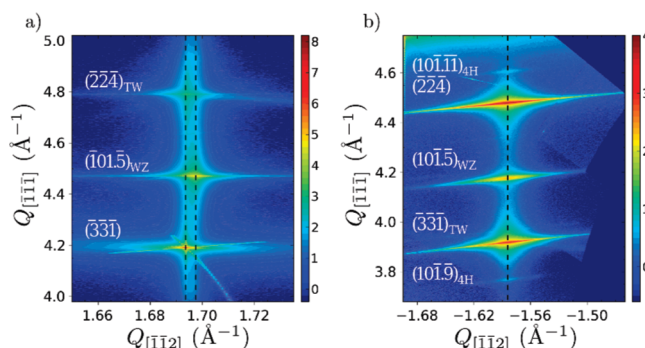


Figure 2. X-ray diffraction data: reciprocal space maps (RSMs) showing the diffracted intensity along an asymmetric crystal truncation rod on a logarithmic scale for sample C2 (InAs) in panel a and sample E2 (InSb) in panel b. In (a) the InAs $(\bar{3}\bar{3}\bar{1})$ substrate, $(\bar{1}01.5)_{\text{WZ}}$, and $(\bar{2}\bar{2}\bar{4})_{\text{TW}}$ wire peaks are visible. Slight in-plane displacement of the WZ peak with respect to the InAs ZB peaks is observed indicating the difference in the in-plane lattice plane spacing. In (b) the RSM shows ZB, ZB_{TW}, WZ, and 4H peaks from the InSb wires. Due to the lattice mismatch between the InSb wires and InAs substrate, the $(\bar{2}\bar{2}\bar{4})$ substrate peak is outside the shown range in panel b, whereas the substrates $(\bar{3}\bar{3}\bar{1})$ peak in panel a overlaps with the scattering signal from the wires.

truncation rod (CTR) at an asymmetric reflection are performed. In this geometry, scattering from planes with a certain angle to the (111) substrate surface is recorded, and from the positions of the Bragg peaks we determine the lattice parameters both along the growth direction and perpendicular to it. Due to the structure factor selection rules and the very similar lattice plane spacings for all polytypes along the $[111]/[000.1]$ direction, their Bragg peaks overlap for symmetrical reciprocal space maps (RSMs), and it is hardly possible to distinguish between the ZB, WZ, and 4H stacking, or to determine the lattice constants accurately. In contrast, scanning along a CTR at an asymmetric reflection, the different structures diffract at separate positions because of the different unit cell sizes and symmetries. As an example, Figure 2 shows the measured RSM from sample C2 with the $(\bar{3}\bar{3}\bar{1})$ substrate Bragg peak, $(\bar{1}01.5)_{\text{WZ}}$ and $(\bar{2}\bar{2}\bar{4})_{\text{TW}}$ wire Bragg peaks in panel a, while panel b shows a similar measurement from sample E2, containing also the Bragg peaks due to 4H segments. For the $(\bar{2}\bar{2}\bar{4})_{\text{TW}}$ Bragg peak, the crystal symmetry and the effect of twin defects are used to isolate the scattering from cubic InAs avoiding overlap with the strong Bragg reflections of the InAs substrate in homoepitaxial wire samples: The $(\bar{2}\bar{2}\bar{4})$ substrate peaks appear in three different azimuths, i.e., 0°, 120°, and 240°. Due to twin boundaries appearing in the NWs, a certain part of the cubic InAs in the NWs is rotated by 180° (equivalent to a 60° rotation) with respect to the substrate lattice. Selecting the proper azimuth, we are thus able to isolate the scattering signal from the cubic InAs segments in the wires. This is denoted by the subscript “TW”. To measure both diffraction signals from $(\bar{2}\bar{2}\bar{4})$ and $(\bar{3}\bar{3}\bar{1})$ peaks, RSMs are measured in two azimuths differing by 180°, which allows at the same time to eliminate any errors in peak position determination arising from possible tilts of the NWs with respect to the substrate. Each of the maps contains at least one sharp substrate Bragg peak with known position, which is used as a reference. The exact peak positions and therefore the lattice constants which are calculated from the Bragg peak positions were determined by fitting a two-dimensional Gaussian to the measured intensities. Although the exact shape of the peak is not Gaussian, the central part dominating the error in the fitting procedure is approximated to a good degree by a Gaussian

Table 2. Average Experimental Results for the Lattice Constants a and c of the Different Polytypes (for ZB/3C the Cubic Values have been Converted using Eq 1)^a

	a (Å)	c (Å)	exptl $(2c)/(pa)$	DFT $(2c)/(pa)$
InAs ZB/3C	4.2837	10.4923	1.6329	$(8/3)^{1/2}$
InAs 4H	4.2780	14.0171	1.6383	1.6384
InAs WZ/2H	4.2742	7.0250	1.6436	1.6436
InSb ZB/3C	4.5801	11.2198	1.6331	$(8/3)^{1/2}$
InSb 4H	4.5753	15.0057	1.6399	1.6387
InSb WZ/2H	4.5712	7.5221	1.6456	1.6449

^a The aspect ratio $(2c)/(pa)$ determined experimentally and as obtained by the DFT calculations is given for 3C and the pH polytypes. The average experimental error found for a single measurement is 0.034% for the a -lattice parameter and 0.025% for the c -lattice parameter.

distribution. For the InSb samples a random tilting of few 0.1° of the wires is observed, leading to a broadening of the Bragg peaks perpendicular to the momentum transfer vector. Therefore, a rotation of the Gaussian peaks in the RSM plane has been included as an additional fitting parameter.

The RSMs were recorded at two laboratory diffractometers and a synchrotron source (beamline BW2 at Hasylab Hamburg). The laboratory experiments were performed using a custom built rotating anode setup with a double bent multilayer mirror and a Ge(220) channel cut monochromator, as well as a PANalytical X'Pert PRO equipped with a sealed tube, parabolic multilayer mirror, and Bartels monochromator. Cu $K\alpha_1$ radiation was used for the measurements. Selected samples were also measured using synchrotron radiation with an energy of 9515 eV. For all the X-ray experiments, a position-sensitive detector was used.

The error of the experimental method was investigated by considering the effects of experimental misalignments, goniometer movement accuracy, detector resolution, and the uncertainty introduced by the fitting procedure. Furthermore the different refraction effects for NWs and the substrate peaks were considered. The error is dominated by geometric effects like detector resolution and the error of the fit. The average error of a single lattice constant measurement is found to be 0.034% for the in-plane lattice constants along $[\bar{1}\bar{1}2]$ and 0.025% along $[111]$, with slightly lower values for the synchrotron measurements due to the better signal-to-noise ratio and increased detector resolution. The confirmation of low defect density in the measured structures by TEM is important, since even if the wires consist only of one hexagonal phase, stacking faults with a stacking ABAB ABC BCBC or ABABA BAC ACAC, could lead to a slight shift of the Bragg peaks observed in X-ray diffraction if these two faults are not present in equal portions. We do, however, not have an experimental indication of one defect type being preferred. This effect can anyhow be ignored if the total defect density is sufficiently low.

For all samples, deviations of the hexagonal lattice constants from the simple geometrically converted values are found. Within the experimental error no deviations between the different samples could be found; therefore only the average of the obtained values will be discussed. The average experimentally determined lattice constants are listed in Table 2. In Figure 3 the deviations from the reference values calculated by $\Delta a = (a - a_{\text{geom},p})/a_{\text{geom},p}$ and $\Delta c = (c - c_{\text{geom},p})/c_{\text{geom},p}$ are shown as function of the hexagonality of the different polytypes. The reference values are the geometrically converted cubic bulk lattice constants $a_c = 6.0583$ Å for InAs and $a_c = 6.4794$ Å for InSb³⁷ scaled by the unit cell size of the polytype.

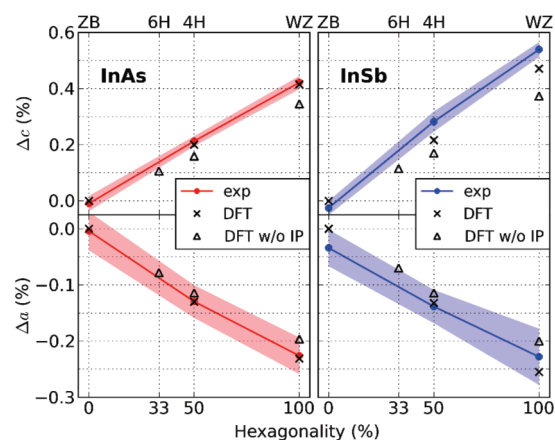


Figure 3. Experimental and theoretical relative deviations Δa and Δc of the lattice parameters from the values of eq 1 are given as function of hexagonality. The colored dots denote the average experimental values and the shaded areas indicate the experimental error of a single measurement. DFT results for internal parameters set to zero (triangles) as well as after optimization (crosses) are shown.

These are calculated by

$$a_{\text{geom},p} = a_c/\sqrt{2} \quad \text{and} \quad c_{\text{geom},p} = a_cp/\sqrt{3} \quad (1)$$

for the pH and pC polytypes. Furthermore the results are compared to theoretically obtained lattice parameters as discussed below. The dots in Figure 3 denote the average values obtained for all samples. The shaded areas indicate the experimental error of a single measurement, while the total error of the average is less than the width of the solid line. The latter is only a guide to the eye, since no real crystal structure exists in between the different polytypes.

In order to investigate the ground-state geometry of the various polytypes by first principles, we use density functional theory (DFT) as it is implemented in the Vienna ab initio simulation package (VASP).^{38,39} Pseudopotentials are generated within the projector-augmented wave (PAW) method,⁴⁰ whereas the 4d states of the cations are treated as valence states.⁴¹ To describe the exchange and correlation energy, we use the local density approximation (LDA), which for the case of III–V semiconductors reproduces the experimental ZB lattice constants to a good degree.⁴² For the plane-wave expansion we use an energy cutoff of 450 eV. The sampling of the Brillouin zone is done via Γ -centered k -point meshes, which are adopted to the unit cells of the different polytypes in order to reach a convergence around 1 meV. The atomic basis within unit cells with internal parameters (IPs) can be constructed from the parameters u, v and w in the Wyckhoff⁴³ positions $(0,0,u)$ and $(\frac{1}{3}, \frac{2}{3}, \frac{1}{2} + u)$ with $u(\text{III}) = 0, u(\text{V}) = \frac{3}{8} + \varepsilon$ in WZ and from the Wyckhoff positions $(0,0,u), (\frac{1}{3}, \frac{2}{3}, v)$, and $(\frac{2}{3}, \frac{1}{3}, w)$ with $u(\text{III}) = 0, u(\text{V}) = \frac{3}{16} + \varepsilon, v(\text{III}) = \frac{1}{4} + \delta, \frac{3}{4} + \delta, v(\text{V}) = \frac{7}{16} + \varepsilon', \frac{15}{16} + \varepsilon', w(\text{III}) = \frac{1}{2},$ and $w(\text{V}) = \frac{11}{16} + \varepsilon$ in 4H. A sketch of the unit cells of 4H and WZ can be found in panels b and c of Figure 4. These internal-cell parameters $\varepsilon, \delta,$ and ε' indicate additional deviations from the ideal bonding tetrahedra.

The equilibrium atomic geometries are obtained by minimizing the total energy E with respect to the lattice constants a and c of the polytypes, as well as with respect to the IPs $\varepsilon, \delta,$ and ε' , taking atomic relaxations within the unit cell under the symmetry constraint of C_{6v}^4 ($P6_3mc$) into account. The influences of finite temperature and of the free energy of the vibrating lattices are neglected.⁴⁴

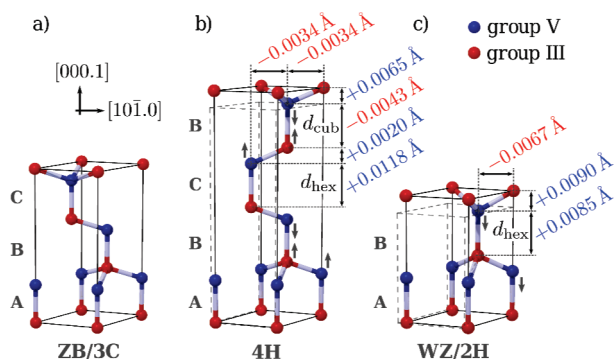


Figure 4. Sketch of the unit cell structures of ZB/3C, 4H, and WZ/2H. The theoretically obtained deformation of the unit cell as a whole and the atomic basis within, exaggerated by a factor of 30, is shown in comparison to the ideal cell constructed from the cubic lattice constant (dashed lines). The numerical values of the unit cell distortions, especially of the bond lengths d_{hex} and d_{cub} , are given for InSb. Qualitatively the same changes were found for InAs. The direction of the displacement of the atoms due to the internal parameters is indicated by arrows.

The ZB reference values obtained by DFT calculations are $a_c = 6.0321$ Å for InAs and $a_c = 6.4542$ Å for InSb. The absolute lattice parameters are influenced by the overbinding tendency due to the description of exchange and correlation within the LDA. However, the error introduced by the LDA is expected to be very similar for the ZB, 4H, and WZ structures, as these structures only differ by third next neighbor distances. Therefore, the underestimation of the lattice constants by less than 0.5% does not play a role since only relative variations Δa and Δc , calculated using the reference values obtained by DFT, are compared with experimental findings.

To determine the equilibrium lattice constants a and c , we calculated the total energy E on a regular (a, c) grid and interpolated the $E(a, c)$ surface within a cubic interpolation scheme. We include the IPs, i.e., the additional degrees of freedom for atomic relaxation, through a three-way optimization: In the first step we perform a $E(a, c)$ interpolation as described above with all IPs set to zero. In the second step we minimize the energy with respect to the IPs, while the lattice parameters a and c are kept fixed. The last step is again a $E(a, c)$ minimization with the IPs of step two, in order to improve the accuracy for the description of the interplay of lattice constants and IPs. Compared to the most accurate multidimensional interpolation, where all parameters (a, c and IPs) are optimized independently, the used three-step procedure scales better concerning the number of IPs and the grid size, thereby reducing the computational effort. Additionally, test calculations for WZ—InAs show that the results of different minimization procedures are close to each other. The lattice constant a is almost the same, while c is slightly increased by ~ 0.002 Å when using the multidimensional interpolation scheme.

Both XRD experiments and the DFT calculations show that deviations from the lattice constants obtained by simple geometrical conversion (eq 1) exist for both InAs and InSb, as shown in Table 2 and Figure 3. The agreement between measurement and calculations is excellent. This holds not only for the sign and order of magnitude of the lattice constant deviations Δa and Δc but also for the absolute values of these deviations. Figure 3 shows the perfect agreement for InAs polytypes, whereas slight deviations between theory and experiment were found for InSb, which could be due to the remaining effects of mutual straining of the different segments or the stronger overbinding tendency of the LDA functional used in the case of InSb.

While the 4H segments are not expected to be strain free, because of their limited segment length of typically 5–15 nm, unexpectedly good agreement was found between theory and experiment. However, if a 4H segment is sandwiched between extended ZB and WZ segments, as is the case here (see Figure 1b), the strain induced by both sides could indeed compensate to zero. Finite element modeling was used to determine the strain state of such sandwiched 4H segments. For the simulations the theoretically obtained lattice parameters from Figure 3 and equal elastic properties of the hexagonal polytypes⁴⁵ were used. It was found that the strain of the 4H structure is antisymmetric along the segment, which can be understood because the WZ segment at the top and ZB segment at the bottom have approximately the opposite lattice mismatch with respect to 4H. The measured lattice parameter represents the average over the extent of the 4H segments, which is virtually equal to the relaxed value, as was confirmed by finite element calculations. This explains the agreement between theory and experiment even for the rather short segments. The experimental and theoretical relative aspect ratios $(2c)/(pa)$ as given in Table 2 are almost the same, with a maximum deviation for 4H—InSb of less than 0.1%. This agreement is astonishing, because the DFT calculations treat ideal bulk polytypes in equilibrium at zero temperature, while XRD studies III—V bilayer stackings in nanowires with real structure, limited dimensions, and influenced by growth kinetics. However, within the experimental error no dependence of the lattice parameters on the wire diameter (samples C1—C3) could be found, indicating that surface effects are negligible. Furthermore, no differences between the samples grown by MOVPE and CBE were found.

Experiment and theory show that the occurrence of hexagonal bilayers tends to stretch the distances of atomic layers parallel to the c axis, while concomitantly the in-plane distances perpendicular to the c axis are reduced. The combination of both effects results in the observed rise of the relative aspect ratio $(2c)/(pa)$ with increasing hexagonality. Part of the aspect ratio change could be traced back to internal structure relaxation, i.e., the influence of internal parameters. Figure 4 shows sketches of the unit cells of the different polytypes, where the theoretically obtained deformation in comparison to the geometrically converted unit cell dimensions (dashed lines) is indicated. For both the WZ and 4H structure the bond length d_{hex} of the hexagonal stacked bilayers is found to be stretched in comparison to the corresponding bond length in the ZB structure. The bond length increases because of the repulsive force of the third next neighbors, which are located closer to each other in the case of a hexagonal stacked layer (see Figure 1c). In contrast to the general increase of the unit cell dimension in the c direction, the bond length d_{cub} of the cubic bilayers in 4H even decreases in comparison to ZB. The DFT calculations further show that the bond angles are also changed by some tenth of a degree, when the stacking changes. The absolute values of the IPs ϵ , δ , and ϵ' are only of the order of 10^{-4} and therefore similar to the case of SiC polytypes^{21,46} and former calculations for GaAs—WZ.^{32,33} Nevertheless, the internal atomic relaxation considerably influences the results, i.e., a careful treatment of the cell IPs is important. For instance, the mentioned inhomogeneity of the bond lengths ($d_{\text{hex}} \neq d_{\text{cub}}$) is directly connected to the IPs because $d_{\text{hex}} - d_{\text{cub}} = (|\epsilon| + |\delta| + |\epsilon'|)c_{4\text{H}}$ holds for the 4H polytypes. Also the deviation of the characteristic bond length d_{hex} is doubled via the displacements due to the IPs. The direction of the displacement of the atoms due to the internal parameters is indicated by arrows in Figure 4. With decreasing hexagonality, the influence of IPs becomes weaker.

To determine the IPs directly from XRD experiments, absolute intensity and shape of a complete set of Bragg peaks need to

be determined.^{46,47} However, in the present case, the shape and intensity of the Bragg peaks from the NWs are influenced by ensemble averaging effects, and only their positions can be evaluated with sufficiently high precision. An alternative technique which is in principle able to determine the IPs experimentally would be extended X-ray absorption fine structure (EXAFS) experiments, where the bond length of a certain kind of atoms is determined. Although the required accuracy in the 10^{-3} Å range was demonstrated, e.g., in thin film experiments,⁴⁸ it is not possible to resolve the minute differences in the bond length of the tetrahedrally coordinated atoms in NWs: The DFT calculations predict that each atom of a certain kind has various neighbors at slightly different distances, so that the obtained coordination shells would strongly overlap and cannot be isolated from each other. Therefore an experimental verification of the IPs is not directly possible in this case. However, about 20% of the calculated change in the lattice parameters a and c can be traced back to the influence of the IPs. These lattice parameters are measured with very high precision, so that the excellent agreement between experiment and theory (see Figure 3) indirectly confirms the IP values.

All geometric changes are clearly proportional to the hexagonality. In the case of 4H with hexagonality of 50%, they are less pronounced in comparison to WZ with 100% hexagonality. This is evident from Figure 4, where it is shown that each hexagonal stacked bilayer contributes to the stretching of the unit cell in the c axis, whereas it reduces the in-plane atomic distances: note that the absolute change of the unit cell size in the c direction is roughly the same for 4H and WZ, while the 4H unit cell contains twice as many layers as the WZ unit cell. The chemical trend is less significant. The relative c lattice constant variation Δc is enhanced with decreasing bond ionicity from InAs to InSb, as shown in Figure 3, while an analogous tendency for Δa could not be observed.

In conclusion, we employed X-ray diffraction to accurately determine the lattice parameters of InAs and InSb polytypes in dependence of the hexagonality. Transmission electron microscopy was used to verify that extended segments of the ZB, WZ, and 4H phase are present and spatially separated. The results show excellent agreement with DFT calculations including the effect of internal parameters, which determine the distortion of the bonding tetrahedra. Both experiments and theoretical results show that the lattice plane spacing is altered when the structure changes from ZB to 4H and WZ and that the simple geometric conversion formulas are not applicable. For the 4H and WZ polytypes of InAs and InSb, we observe an increase of the (000.1) lattice plane spacing in the c direction by approximately 0.2–0.25% and 0.4–0.5%, respectively. The variation of the in-plane lattice constant shows the inverse behavior and was found to be decreased by approximately 0.12% and 0.25% for the 4H and WZ structures. These accurate structural data enable precise calculations of the band structure and band alignment of the hexagonal polytypes. This will be essential to understand the electronic and optical properties of advanced pure crystal phase and polytypic III–V nanowire devices.

■ ASSOCIATED CONTENT

S Supporting Information. Animation of the unit cell structures of ZB/3C, 4H, and WZ/2H as well as their deformations, showing (exaggerated by a factor of 30) the deviations of the structure obtained by geometric conversion, similar to what is shown in Figure 4. This material is available free of charge via the Internet at <http://pubs.acs.org>.

■ AUTHOR INFORMATION

Corresponding Author

*E-mail: dominik.kriegner@jku.at; christian.panse@uni-jena.de.

■ ACKNOWLEDGMENT

The authors thank the staff at BW2 HasyLab (D. Novikov) for assistance with the beamline setup and E. Vorhauer and F. Binder for technical assistance with the laboratory setups. We acknowledge the financial support from FWF Vienna (SFB025 IR-ON) and the EC (AMON-Ra, 214814, ELISA, 226716 and ETSF, 211956). Part of this work was supported by the Nanometer Structure Consortium at Lund University (nmC@LU), the Swedish Foundation for Strategic Research (SSF), the Swedish Research Council (VR), and the Knut and Alice Wallenberg Foundation. We gratefully acknowledge the use of the TEM facilities at the Center for Electron Nanoscopy at the Technical University of Denmark.

■ REFERENCES

- (1) Thelander, C.; Agarwal, P.; Brongersma, S.; Eymery, J.; Feiner, L.; Forchel, A.; Scheffler, M.; Riess, W.; Ohlsson, B.; Gösele, U.; Samuelson, L. *Mater. Today* **2006**, *9*, 28–35.
- (2) Lieber, C. M.; Wang, Z. L. *MRS Bull.* **2007**, *32*, 99.
- (3) Kitauchi, Y.; Kobayashi, Y.; Tomioka, K.; Hara, S.; Hiruma, K.; Fukui, T.; Motohisa, J. *Nano Lett.* **2010**, *10*, 1699–1703.
- (4) Spirkoska, D.; et al. *Phys. Rev. B* **2009**, *80*, No. 245325.
- (5) Dheeraj, D. L.; Patriarche, G.; Zhou, H.; Hoang, T. B.; Moses, A. F.; Grønsberg, S.; van Helvoort, A. T. J.; Fimland, B.; Weman, H. *Nano Lett.* **2008**, *8*, 4459–4463.
- (6) Caroff, P.; Dick, K. A.; Johansson, J.; Messing, M. E.; Deppert, K.; Samuelson, L. *Nat. Nanotechnol.* **2009**, *4*, 50–55.
- (7) Dick, K. A.; Thelander, C.; Samuelson, L.; Caroff, P. *Nano Lett.* **2010**, *10*, 3494–3499.
- (8) Mandl, B.; Dick, K. A.; Kriegner, D.; Keplinger, M.; Bauer, G.; Stangl, J.; Deppert, K. *Nanotechnol.* **2011**, *22*, 145603.
- (9) Algra, R. E.; Verheijen, M. A.; Borgstrom, M. T.; Feiner, L.-F.; Immink, G.; van Enkevort, W. J. P.; Vlieg, E.; Bakkers, E. P. A. M. *Nature* **2008**, *456*, 369–372.
- (10) Soshnikov, I.; Cirlin, G.; Sibirev, N.; Dubrovskii, V.; Samsonenko, Y.; Litvinov, D.; Gerthsen, D. *Tech. Phys. Lett.* **2008**, *34*, 538–541.
- (11) Joyce, H. J.; Wong-Leung, J.; Gao, Q.; Tan, H. H.; Jagadish, C. *Nano Lett.* **2010**, *10*, 908–915.
- (12) Krogstrup, P.; Popovitz-Biro, R.; Johnson, E.; Madsen, M. H.; Nygård, J.; Shtrikman, H. *Nano Lett.* **2010**, *10*, 4475–4482.
- (13) Shtrikman, H.; Popovitz-Biro, R.; Kretinin, A.; Heiblum, M. *Nano Lett.* **2009**, *9*, 215–219.
- (14) Shtrikman, H.; Popovitz-Biro, R.; Kretinin, A.; Houben, L.; Heiblum, M.; Bukala, M.; Galicka, M.; Buczko, R.; Kacman, P. *Nano Lett.* **2009**, *9*, 1506–1510.
- (15) Zhang, L.; Luo, J.-W.; Zunger, A.; Akopian, N.; Zwiller, V.; Harmand, J.-C. *Nano Lett.* **2010**, *10*, 4055–4060.
- (16) Akiyama, T.; Yamashita, T.; Nakamura, K.; Ito, T. *Nano Lett.* **2010**, *10*, 4614–4618.
- (17) Trägårdh, J.; Persson, A. I.; Wagner, J. B.; Hessman, D.; Samuelson, L. *J. Appl. Phys.* **2007**, *101*, No. 123701.
- (18) Zardo, I.; Conesa-Boj, S.; Peiro, F.; Morante, J. R.; Arbiol, J.; Uccelli, E.; Abstreiter, G.; Fontcuberta i Morral, A. *Phys. Rev. B* **2009**, *80*, No. 245324.
- (19) Akopian, N.; Patriarche, G.; Liu, L.; Harmand, J.-C.; Zwiller, V. *Nano Lett.* **2010**, *10*, 1198–1201.
- (20) Pemasiri, K.; Montazeri, M.; Gass, R.; Smith, L. M.; Jackson, H. E.; Yarrison-Rice, J.; Paiman, S.; Gao, Q.; Tan, H. H.; Jagadish, C.; Zhang, X.; Zou, J. *Nano Lett.* **2009**, *9*, 648–654.

- (21) Käckell, P.; Wenzien, B.; Bechstedt, F. *Phys. Rev. B* **1994**, *50*, 17037–17046.
- (22) Takahashi, K.; Morizumi, T. *Jpn. J. Appl. Phys.* **1966**, *5*, 657–662.
- (23) Mandl, B.; Stangl, J.; Mårtensson, T.; Mikkelsen, A.; Eriksson, J.; Karlsson, L. S.; Bauer, G.; Samuelson, L.; Seifert, W. *Nano Lett.* **2006**, *6*, 1817–1821.
- (24) Bauer, J.; Pietsch, U.; Davydok, A.; Biermanns, A.; Grenzer, J.; Gottschalch, V.; Wagner, G. *Appl. Phys. A: Mater. Sci. Process.* **2009**, *96*, 851–859.
- (25) Mariager, S. O.; Lauridsen, S. L.; Dohn, A.; Bovet, N.; Sørensen, C. B.; Schlepütz, C. M.; Willmott, P. R.; Feidenhans'l, R. *J. Appl. Crystallogr.* **2009**, *42*, 369–375.
- (26) We use Miller indices (hkl) and Bravais indices and ($hki.l$) with $i = -h - k$ to denote hexagonal structures.
- (27) Zanolli, Z.; Fuchs, F.; Furthmüller, J.; von Barth, U.; Bechstedt, F. *Phys. Rev. B* **2007**, *75*, No. 245121.
- (28) De, A.; Pryor, C. E. *Phys. Rev. B* **2010**, *81*, No. 155210.
- (29) Feynman, R. P. *Phys. Rev.* **1939**, *56*, 340–343.
- (30) Lawaetz, P. *Phys. Rev. B* **1972**, *5*, 4039–4045.
- (31) McMahon, M. I.; Nemes, R. J. *Phys. Rev. Lett.* **2005**, *95*, No. 215505.
- (32) Yeh, C.-Y.; Lu, Z. W.; Froyen, S.; Zunger, A. *Phys. Rev. B* **1992**, *46*, 10086–10097.
- (33) Mujica, A.; Needs, R. J.; Muñoz, A. *Phys. Rev. B* **1995**, *52*, 8881–8892.
- (34) Ercolani, D.; Rossi, F.; Li, A.; Roddaro, S.; Grillo, V.; Salviati, G.; Beltram, F.; Sorba, L. *Nanotechnology* **2009**, *20*, No. 505605.
- (35) Fröberg, L. E.; Seifert, W.; Johansson, J. *Phys. Rev. B* **2007**, *76*, No. 153401.
- (36) Mandl, B.; Stangl, J.; Hilner, E.; Zakharov, A. A.; Hillerich, K.; Dey, A. W.; Samuelson, L.; Bauer, G.; Deppert, K.; Mikkelsen, A. *Nano Lett.* **2010**, *10*, 4443–4449.
- (37) Madelung, O. *Semiconductors: data handbook*; Springer: Berlin, 2004.
- (38) Kresse, G.; Furthmüller, J. *Comput. Mater. Sci.* **1996**, *6*, 15–50.
- (39) Hobbs, D.; Kresse, G.; Hafner, J. *Phys. Rev. B* **2000**, *62*, 11556–11570.
- (40) Kresse, G.; Joubert, D. *Phys. Rev. B* **1999**, *59*, 1758–1775.
- (41) Kim, Y.-S.; Hummer, K.; Kresse, G. *Phys. Rev. B* **2009**, *80*, No. 035203.
- (42) Haas, P.; Tran, F.; Blaha, P. *Phys. Rev. B* **2009**, *79*, No. 085104.
- (43) Wyckhoff, R. *Crystal Structures*; Interscience Publishers: New York, 1964; Vol. 1.
- (44) This approach led to to good agreement with available experimental data for SiC polytypes, as is shown in ref 21.
- (45) Martin, R. M. *Phys. Rev. B* **1972**, *6*, 4546–4553.
- (46) Bauer, A.; Kräusslich, J.; Dressler, L.; Kuschnerus, P.; Wolf, J.; Goetz, K.; Käckell, P.; Furthmüller, J.; Bechstedt, F. *Phys. Rev. B* **1998**, *57*, 2647–2650.
- (47) Bechstedt, F.; Käckell, P.; Zywietz, A.; Karch, K.; Adolph, B.; Tenelsen, K.; Furthmüller, J. *Phys. Status Solidi B* **1997**, *202*, 35–62.
- (48) Kuwahara, Y.; Oyanagi, H.; Shioda, R.; Takeda, Y.; Yamaguchi, H.; Aono, M. *Jpn. J. Appl. Phys.* **1994**, *33*, 5631.